Density equilibration near the liquid-vapor critical point of a pure fluid. II. Coexisting phases for $T<T_c$

Fang Zhong and Horst Meyer
Department of Physics, Duke University, Durham, North Carolina 27708-0305
(Received 9 November 1995; revised manuscript received 30 January 1996)

Measurements were carried out on the density change $\delta\rho(t)$ in a pure fluid (^{3}He) after a small step change in the temperature of its container. The sample fluid was kept at constant average densities $\Delta\overline{\rho}$ and in the coexisting liquid and vapor phases below the critical temperature T_c. The measurements were performed via two superposed capacitive sensors. At temperatures far below T_c, the equilibration in the liquid and vapor phases, measured, respectively, by the top and bottom sensors, are found to proceed very differently. As T_c is approached, this difference diminishes; both the measured effective relaxation times level off and join smoothly the data obtained above T_c. This coexisting liquid-vapor system of ^{3}He is simulated in one dimension. The results are presented for the spatial and temporal evolution of temperature and density in the fluid following a temperature step of the enclosure. The profiles $\delta\rho(t)$ and their effective relaxation times are compared with the experimental observations in both phases. There is a qualitative agreement between the simulation and experiment for $(T_c-T)/T_c \lesssim 10^{-3}$, and the quantitative differences further away from T_c are discussed. The results of experimental measurements and of computer simulations along isotherms are discussed and lead to complementary information on the equilibration dynamics as a function of average density. The asymptotic relaxation times obtained from simulation and from a formula based on the average thermal diffusivity of the entire fluid sample are compared and discussed, both for normal gravity, and also under microgravity conditions where both diverge as T_c is approached. [S1063-651X(96)02606-2]

PACS number(s): 44.10.+i, 05.70.Jk, 64.60.−i, 66.10.Cb

I. INTRODUCTION

Assessing the equilibrium state of thermostatic properties and the steady state of transport properties is particularly important near the critical point of a pure fluid. Here the critical slowing down due to the diminishing thermal diffusivity becomes an important factor during relaxation between different states of equilibrium. It is important to understand the equilibration dynamics of the various thermodynamic variables, such as temperature and density, in particular in connection with experimental investigations of critical phenomena under microgravity conditions [1–5].

In our first paper [6] we described experiments and computer simulations of density equilibration above the critical point following a stepwise temperature change of the fluid enclosure. The fluid selected for these studies is ^{3}He because of the past extensive studies in this laboratory of both static and transport properties [7,8]. The critical parameters are $T_c=3.310$ K (T_{62} scale) or 3.316 K (T_{76} scale), $\rho_c=0.0414$ g/cm^3, and $P_c=1.15\times10^6$ dyn/cm^2. The results of the earth-bound experiments with ^{3}He (gravitational acceleration g_0) [6] show the ''piston effect'' and the effect of stratification on the temporal density profile $\rho(z,t)$. The computer simulations were also carried out at normal gravity g_0 and with the average density $\overline{\rho}$ and initial and final temperatures that are similar to the experiments. Hence a direct comparison between experiments and predictions could be made. There was good agreement in the shape and amplitude of the density changes, but the computed equilibration time scale was found to diverge more strongly than the experimental one as T_c was approached. For the reduced temperatures $\epsilon\equiv(T-T_c)/T_c$, where the stratification profile in the cell becomes nonlinear, both the experimental and computed time scales level off to a constant value as T_c is approached closer.

During the same series of experiments, we conducted a similar systematic investigation on the equilibration in the coexisting phases below T_c. In this paper we give an account of these results, some of which were presented in a preliminary form elsewhere [9,10]. A computer simulation on the temporal and the spatial evolution of this two-phase system including the interface motion will be compared with the experimental results.

In Sec. II of this paper, fluid equilibration, convection effects, and equation of state near the liquid-vapor critical point are briefly reviewed, and in Sec. III, the equations that form the basis for the computer simulation are presented. The instrumentation and the experimental procedures are reviewed and described in Sec. IV. The results and discussions for equilibration along the critical isochore and also along two isotherms—both from experiments and from simulation—are presented in Sec. V. In the Appendixes, the spatial profile of equilibrium properties under the influence of gravity is presented at several temperatures. The calculations of the specific heat and thermal diffusivity in the two-phase system is outlined. The numerical simulation procedures are presented and the results of the computer simulation of the interface motion are shown.

II. EQUILIBRATION NEAR THE CRITICAL POINT: A SHORT BACKGROUND

A. Single phase

We consider the problem of the equilibration of a fluid at constant average density $\overline{\rho}$, kept in a flat cell bounded by two

parallel horizontal plates, after a stepwise temperature change ΔT of the enclosure. The plates are assumed to have a very high thermal conductivity. Onuki and Ferrell [11] explained the fast temperature equilibration observed in the single phase of a fluid above the critical point. Here the expansion within the boundary layers due to the rising wall temperature compresses the bulk fluid away from the wall, transferring energy adiabatically from the boundary to interior. This so-called ''piston effect'' changes the temperature at the fluid's interior much faster than if the equilibration was achieved only via thermal diffusion. In the absence of gravity, the equilibration of the supercritical fluid will then show three regimes and will have two characteristic time constants.

(a) The first regime is due to the piston effect. Within a time scale of

$$t_1=\frac{h^2}{4\gamma^2 D_T} \tag{1}$$

the temperature inside the fluid is raised homogeneously from T_0 to $T_0+a\Delta T$ with $a\sim 0.6$ for ^{3}He [based on our one-dimensional (1D) computer simulation for ^{3}He]. Here $D_T\equiv\lambda/\rho C_P$ is the thermal diffusivity, λ is the conductivity, and $\gamma\equiv C_P/C_V$ is the ratio of specific heat at constant pressure over specific heat at constant volume. The piston effect also raises sharply the density inside the fluid to a value slightly above $\overline{\rho}$ and introduces strong density gradients at the two horizontal boundaries.

(b) In the intermediate regime, the temperature inhomogeneity decays with time as $t^{-1/2}$ and the density gradients at the boundaries propagate into the interior of the fluid with decaying amplitude as time increases.

(c) In the diffusive regime, both temperature and density throughout the fluid approach their equilibrium value with a characteristic time $\tau=(h^2/4\pi)D_T^{-1}$ assuming $\gamma\gg 1$. For ^{3}He with $\Delta\overline{\rho}=0$ and $h=0.43$ cm at $\epsilon=1\times10^{-2}$, $t_1=0.35$ s and $\tau=460$ s.

B. Coexisting phases

We expect the piston effect to exist in a coexisting two-phase system. However, we are not certain at present on how the impedance to the pressure waves at the meniscus would influence the piston effect. Additionally we anticipate that the magnitude of the piston effect in each phase depends strongly on the respective thermodynamic coefficients in the two phases.

For the two coexisting phases, we use the expression

$$t_g\sim\frac{h^2}{4(D_T)_b}\left[\frac{\overline{C_V}}{(C_P)_b}\right]^2 \tag{2}$$

for the characteristic piston effect time t_g (instead of t_1) where inhomogeneity due to gravity (see Eq. (56) of [11] and also Fig. 2 of [6]) is taken into account. Here $\overline{C_V}$ is the spatial average of local C_V over the whole fluid layer and $(D_T)_b$ and $(C_P)_b$ are the properties at the fluid boundaries prior to the temperature change. (In the calculation of $\overline{C_V}$ we do not include here the effect of the mass crossing the meniscus since it is mostly an effect that is significant at $t\gg t_g$. For the complete calculation of $\overline{C_V}$ see Ref. [12].) We use the average of the t_g obtained from the $(D_T)_b$ and $(C_P)_b$ at the liquid and vapor boundaries.

Onuki and Ferrell [11] have also given another characteristic time, called crossover time t_{g-l}, for a two-phase system,

$$t_{g-l}=\gamma t_1. \tag{3}$$

They predicted that the main inhomogeneity in the fluid system is to exist near the interface for $t\gtrsim t_{g-l}$. This is to be compared with the spatial temperature profiles obtained from simulations (see Sec. V). Inserting the relevant thermodynamic parameters for ^{3}He with $\Delta\overline{\rho}=0$ and $h=0.43$ cm, we obtain $t_g=1.2$, 0.10, and 0.012 s and $t_{g-l}=42$, 37, and 26 s for $|\epsilon|=1\times10^{-2}$, 1×10^{-3}, and 2×10^{-4}.

III. NUMERICAL CALCULATION

In this paper, P, T, and ρ are all scaled by their respective values at the critical point. In Ref. [6], we presented the governing equations in one dimension for the change of pressure, temperature, and density in a homogeneous fluid, where the flow velocity was neglected. The coupled equations were solved numerically in the laboratory coordinate $\{z\}$. When a material coordinate $\{z'\}$ is introduced [13] where

$$z'=\int_0^z \rho(x,t)dx, \tag{4}$$

the same set of equations as in [6] are transformed to [14]

$$\frac{\partial T}{\partial t}-\left[1-\frac{1}{\gamma}\right]\left(\frac{\partial T}{\partial P}\right)_\rho\frac{\partial P}{\partial t}=\frac{1}{c_P}\frac{\partial}{\partial z'}\left[\rho\lambda\frac{\partial T}{\partial z'}\right], \tag{5}$$

$$P(z',t)=P(z'=0,t)+gz'. \tag{6}$$

The pressure change rate at fixed z' in Eq. (5) is independent of z' based on Eq. (6), which can be calculated from

$$\frac{\partial P}{\partial t}=\frac{-\int_0^M\frac{1}{\rho^2}\left(\frac{\partial\rho}{\partial T}\right)_P\frac{\partial T}{\partial t}dz'}{\int_0^M\frac{1}{\rho^2}\left(\frac{\partial\rho}{\partial P}\right)_T dz'}. \tag{7}$$

Here M is the total mass of the fluid. Equation (7) is derived using the differential equation of state

$$\frac{\partial\rho}{\partial t}=\left(\frac{\partial\rho}{\partial T}\right)_P\frac{\partial T}{\partial t}+\left(\frac{\partial\rho}{\partial P}\right)_T\frac{\partial P}{\partial t}, \tag{8}$$

with the condition of total volume being constant. Boukari *et al.* [14] have used Eqs. (5)–(7) to study the equilibration process of Xe near its critical point. We double-checked our simulations published in [6] with Eqs. (5)–(7) and came out with the same numerical results.

In this paper, we adapt Eqs. (5)–(7) to a two-phase system, taking into account the mass transport across the meniscus. A report of computer simulation for the coexisting phases has been published by Straub and Eicher [15] for

CO_2 with $\Delta\overline{\rho}=0$ and for $\epsilon=-1\times10^{-2}$. In Sec. V, we shall discuss their results together with ours.

In a two-phase system, the total volume is the sum of the liquid and vapor volumes,

$$V=\int_0^{z_m'}\frac{dz'}{\rho_{\rm vap}}+\int_{z_m'}^{M}\frac{dz'}{\rho_{\rm liq}}, \tag{9}$$

where the cross section is taken to be unity and z_m' is the total mass of the vapor phase and a function of time. Taking the time derivative of Eq. (9) and using the differential equation of state, Eq. (8), we have

$$\frac{\partial P}{\partial t}=\frac{-\int_0^M\frac{1}{\rho^2}\left(\frac{\partial\rho}{\partial T}\right)_P\frac{\partial T}{\partial t}dz'+\left(\frac{1}{\rho_{\rm vap}}-\frac{1}{\rho_{\rm liq}}\right)_m\frac{\partial z_m'}{\partial t}}{\int_0^M\frac{1}{\rho^2}\left(\frac{\partial\rho}{\partial P}\right)_T dz'}. \tag{10}$$

Here $\partial z_m'/\partial t$ is the net mass flux across the meniscus and together with latent heat Δh it yields the total heat generated at the meniscus,

$$Q_l=-\Delta h\frac{\partial z_m'}{\partial t}. \tag{11}$$

This heat source ($Q_l>0$) or sink ($Q_l<0$) equals the difference of heat currents from both sides of the meniscus. Thus we have

$$\frac{\partial z_m'}{\partial t}=\frac{1}{\Delta h}\left[\rho\lambda\frac{\partial T}{\partial z'}\bigg|_{\rm liquid}-\rho\lambda\frac{\partial T}{\partial z'}\bigg|_{\rm vapor}\right]_m. \tag{12}$$

Equations (5), (10), and (12) give us a complete description of the equilibration process in the two-phase system.

To solve these equations, we assume that the phase transition occurs only at the meniscus. At any other location in the fluid, especially within boundary layer, the liquid can be superheated and the vapor can be subcooled into the region between the coexistence and spinodal curves. The detailed procedures to solve numerically Eqs. (5), (10), and (12) are given in Appendix B.

Although the flow velocity is implicitly included in Eqs. (5) and (6) with the acceleration and viscous dissipation neglected, our approach to solve these equations in one dimension prevents us from studying numerically the convective flow motion since convection in one dimension is excluded. Zappoli and co-workers [16] have carried out a detailed numerical calculation of mass transport in a square cavity filled with supercritical CO_2 for $\epsilon=3\times10^{-3}$, where they studied the interplay of the piston effect, convective transport, and thermal diffusion. A detailed discussion on the convection effects will be given in Appendix A.

In our model of thermal equilibration, the vapor phase in the top part of the cell is separated from the liquid by a flat horizontal meniscus and for the sake of simplicity no account is taken of effects from the surface tension. In reality, as the critical point is approached, the surface tension of ^{3}He vanishes just like in other classical fluids and confirms the predictions [17]. Under normal gravity, these effects cause the meniscus to curve upward near boundaries, which leads in the experimental cell to a departure from the flat surface assumed in the calculations. Under near-zero gravity conditions, it is known that bubbles of vapor surrounded by liquid are formed below T_c [18].

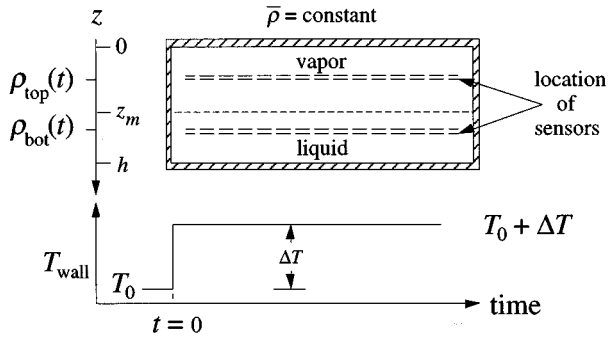

FIG. 1. Top: schematic view of the flat cell for a fluid density measurement at two superposed locations. The dashed line represents the meniscus. Bottom: temperature step sequence ΔT of the cell versus time t.

IV. EXPERIMENT

Here we outline briefly the experimental methods and procedures and refer for more details to [6]. The fluid sample is enclosed in a flat cylindrical cell of oxygen-free high-conductivity copper, with a fluid layer height of $h=4.3$ mm and a diameter of 3.3 cm. The cell is shown schematically in Fig. 1. Inside the cell are two rigidly supported horizontal capacitors separated by 2.1 mm center to center. Each capacitor has a gap of 0.13 mm between two perforated stainless steel blades of 0.13 mm thickness. It measures the dielectric constant ϵ^* of the fluid, from which the local densities $\rho_{\rm top}$ and $\rho_{\rm bot}$ are obtained via the Clausius-Mossotti relation. Such determination has a resolution of $\delta\rho/\rho=2\times10^{-6}$, which is conditioned by the stability and electronic noise of the detection system. During a series of measurements, the average density $\overline{\rho}$ in the cell is kept constant. A sequence of computer-programmed small temperature steps ΔT of the fluid enclosure is produced as shown in Fig. 1. Once the density equilibrium following a previous ΔT step has been reached within the experimental resolution, the next step is implemented. Steps of opposite directions are used to test the reversibility of the process and to search for possible effects from convection. The temperature calibration and the location of T_c and of ρ_c have been described in [6].

When two phases coexist in the cell and stratification in each phase is negligible, a change in temperature from the initial $T_i=T_0$ to the final $T_f=T_0+\Delta T$ temperature, with $T_f>T_i$, will have the equilibrium value of $\rho_{\rm liq}$ decreased and that of $\rho_{\rm vap}$ increased. The equilibrium values of the density in each phase can be described by the equation of state of the coexisting curve (CXC) for $|\epsilon|\lesssim0.1$,

$$\Delta\rho_{\rm CXC}=\pm B|\epsilon|^\beta. \tag{13}$$

Here $\Delta\rho\equiv(\rho-\rho_c)/\rho_c$ is reduced density, $\beta=0.355$ is the effective critical exponent for ^{3}He, and the signs of the amplitude B ($+$ and $-$) are for the liquid and vapor. Close to

T_c, besides these changes in $\rho_{\rm liq}$ and $\rho_{\rm vap}$, a stronger stratification at T_f will increase $\rho_{\rm liq}$ and decrease $\rho_{\rm vap}$ at the locations away from the meniscus.

Under equilibrium conditions, the vertical location z_m of the meniscus (see Fig. 1) for a sample of an average reduced density $\Delta\overline{\rho}$ at a given $|\epsilon|$ can be approximated by

$$z_m=\frac{h}{2}\left[1-\frac{\Delta\overline{\rho}}{|\Delta\rho_{\rm CXC}|}\right], \tag{14}$$

where $\Delta\rho_{\rm CXC}$ is calculated from Eq. (13). Equation (14) is derived from the mass conservation and assumes constant density in each phase (a more accurate result can be obtained from the cubic model when stratification in each phase is included). Since $|\Delta\rho_{\rm CXC}|$ decreases for a positive ΔT, the meniscus ends up at a higher (lower) location than its initial one for a fluid of $\overline{\rho}>\rho_c$ ($\overline{\rho}<\rho_c$). Given the coexistence curve of Eq. (13), Eq. (14) expresses a well known fact that the meniscus is located at $z_m=h/2$ for the fluid of $\overline{\rho}=\rho_c$ regardless of temperature, namely, the ''rectilinear diameter'' has a slope of zero, which is very nearly so the case for ^{3}He [7].

V. RESULTS AND DISCUSSION

In this section we present first the numerical simulations for the fluid sample along the critical isochore $\Delta\overline{\rho}=0$, following the temperature step of the fluid enclosure, and we compare them with the experimental observations. Then we will use the same procedure for the fluid along isotherms, i.e., with $\Delta\overline{\rho}\neq 0$, where the meniscus changes to a different location at the final equilibrium temperature. These results will bring interesting complementary information to that obtained along $\Delta\overline{\rho}=0$.

A. Critical isochore

1. Nonstratified coexisting phases

For $|\epsilon|>5\times10^{-3}$, density stratification in each phase is negligible due to the small compressibility; but the large density difference between the two-phases causes distinct respective dynamics. Figure 2 shows spatial profiles of the changes $\delta\epsilon(z,t)$ and $\delta\rho(z,t)$ at several time instants for $\epsilon=-1\times10^{-2}$ and a step $\Delta\epsilon=\Delta T/T_c=1.2\times10^{-5}$.

Because of the larger coefficient of $(\partial T/\partial P)_s$ in Eq. (5), the vapor phase is more efficient in converting energy adiabatically than is the liquid phase. Thus a nearly uniform pressure change in the cell results in a larger temperature change in the vapor phase than in the liquid. We can see from Fig. 2 that the piston effect dominates the temperature equilibration up to at least $t=10$ s, for $\epsilon=-1\times10^{-2}$. After $t>10$ s, and starting from the cell boundary ($z=0$), the temperature in the vapor phase passes beyond the final equilibrium value. This is the result of the adiabatic energy conversion due to the increasing pressure in the cell. A similar phenomenon has been predicted during the simulations for $T>T_c$ when stratification is strong [6,14].

Based on the derivation of Eq. (3) by Onuki and Ferrell [11], we equal the temperature difference between the middle of the liquid and vapor phases to that between the meniscus and its final equilibrium value. This gives us the

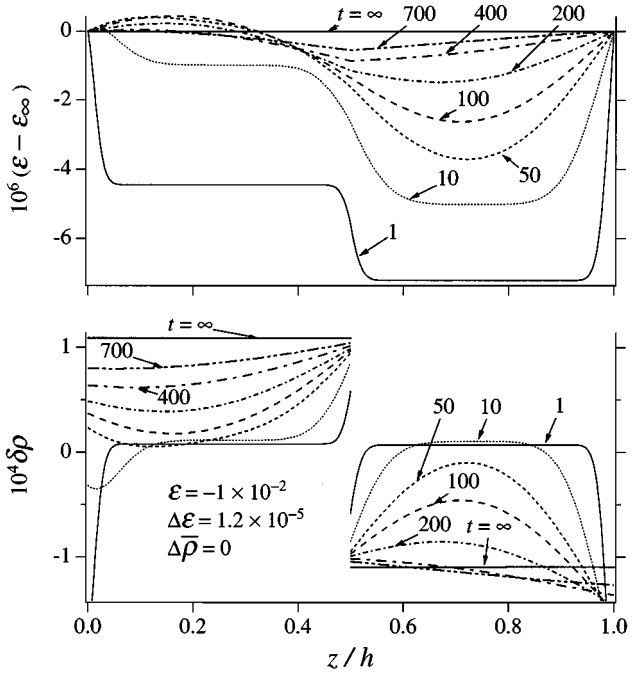

FIG. 2. Simulated spatial profiles of $\epsilon-\epsilon_\infty$ and $\delta\rho\equiv\rho-\rho_0$ for the coexisting phases of ^{3}He on critical isochore versus z at various times (in s) after a temperature step $\Delta\epsilon=1.2\times10^{-5}$ at $\epsilon=-1\times10^{-2}$.

crossover time t_{g-l} of 4 s from the simulation, compared to $t_{g-l}=42$ s from Eq. (3). A large inhomogeneity in the fluid system exists throughout the liquid and vapor phases for $t\gtrsim t_{g-l}$, which differs from the predictions of Ref. [11]. We note that the t_{g-l} given by Eq. (3) is closely related to the time when the temperature in the vapor phase increases beyond its final equilibrium value due to the adiabatic heating. This observation holds over the whole investigated temperature range under microgravity condition.

The large temperature gradients close to the cell boundaries lead to large density gradients there. The density discontinuity at the meniscus produces another boundary layer and accelerates the density equilibration towards its final value near the meniscus at times up to the order of τ. The density transients at different locations in the cell can be understood in terms of the differential equation of state, Eq. (8), and of the boundary layers diffusing into the interior of each phase. During the time interval when the piston effect dominates the temperature equilibration, the simulation shows that the density rises quickly in the interior of both the vapor and liquid phases ($\delta\rho\approx+1\times10^{-5}$) due to the compression from the boundary layers. This is similar to that for the homogeneous fluid at $T>T_c$. After the piston effect decays, the larger temperature gradients remaining in the liquid leads to a larger density change there than in the vapor. This is clearly shown by comparing the density changes in both phases at times, say, $t=100$ and 200 s. Since the final density changes are $\delta\rho_{\rm vap}(t=\infty)=-\delta\rho_{\rm liq}(t=\infty)$, but the initial density changes within the boundary layers have same sign, the expansion of the boundary layers affects differently the density transient in the two phases, making the density transient in the liquid phase appear faster than in the vapor phase.

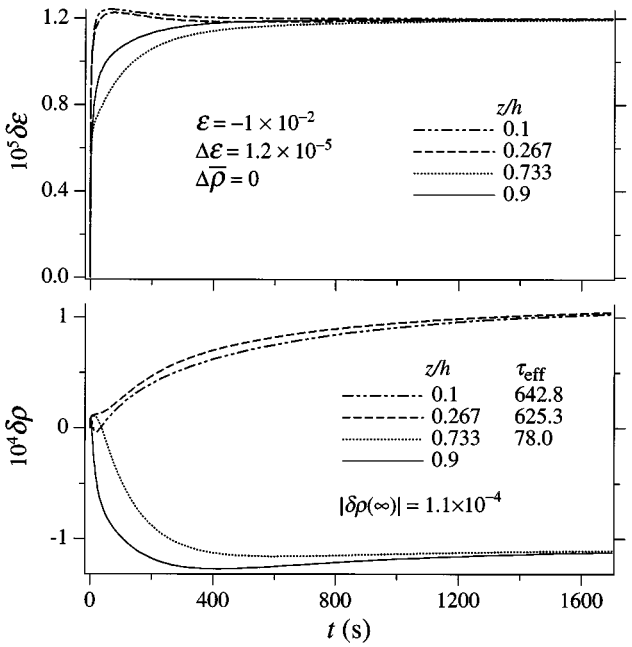

FIG. 3. Simulated temporal profiles of $\delta\epsilon \equiv \epsilon - \epsilon_0$ and $\delta\rho$ for the coexisting phases of ^{3}He on the critical isochore at the two sensor locations ($z/h = 0.267$ and 0.733) and two locations close to the cell boundaries, following a temperature step $\Delta\epsilon = 1.2\times10^{-5}$ at $\epsilon = -1\times10^{-2}$.

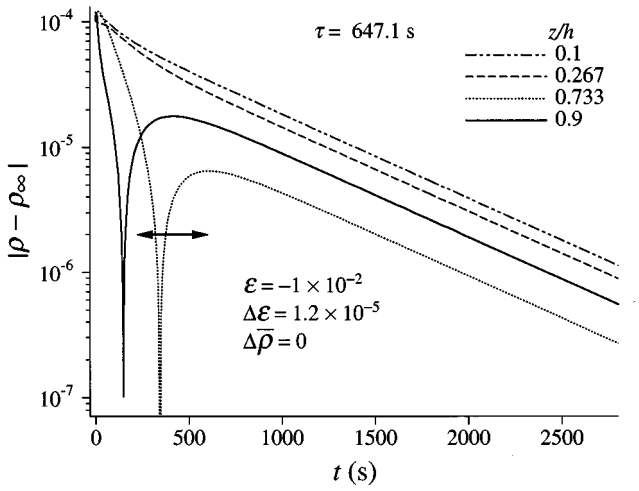

FIG. 4. Semilogarithmic plot of $|\rho(t) - \rho(\infty)|$ taken at the two sensor locations ($z/h = 0.267$ and 0.733) and the two locations close to cell boundaries for $\Delta\epsilon = 1.2\times10^{-5}$ at $\epsilon = -1\times10^{-2}$. The double-arrowed line marks the limit of experimental resolution in $\delta\rho$.

In Fig. 3 we present the temporal profiles of the temperature change $\delta\epsilon$ and $\delta\rho$ at the four locations as indicated in the graph, of which the second and third are the density sensor locations in our experimental setup. When the temperature in the middle reaches $0.6\Delta T$, the time is found to be 1.7 s, which is to be compared with $t_g = 1.2$ s calculated from Eq. (2). Figure 3 shows that in the vapor phase, after the initial sharp changes due to the piston effect, the $\delta\rho(t)$ curves for both $z/h = 0.1$ and 0.267 tend towards the equilibrium value in a nearly exponential fashion. By contrast, in the liquid phase the transients $\delta\rho(t)$ for $z/h = 0.733$ and even more so for $z/h = 0.9$ pass beyond the value $\delta\rho(\infty) = 1.1\times10^{-4}$ before slowly approaching the limiting value from below. The ''undershoot'' beyond the equilibrium value is more strikingly shown in Fig. 4 when the simulated $|\rho(t) - \rho(\infty)|$ is plotted vs time on a semilogarithmic scale. This figure also shows that there exists indeed a spatially independent asymptotic relaxation time with $\tau = 647$ s. In this paper, we use the word ''undershoot'' (or ''overshoot'') to describe a transient passage of the temperature or density *below* (or *above*) its final equilibrium value.

The simulation results obtained by Straub and Eicher [15] for CO_2 at $\epsilon = 1\times10^{-2}$ are consistent with those presented for ^{3}He in Figs. 2 and 3. They show in particular similar amplitudes for the initial changes in the respective temporal profiles of both $\rho_{vap}(t)$ and $\rho_{liq}(t)$.

In Fig. 5 the corresponding experimental observation sequence is shown, where both positive and negative temperature steps of equal magnitude were taken. It can be clearly seen that the temporal density profiles are entirely reversible upon changing the sign of $\Delta\epsilon$. The effective relaxation times indicated for each relaxation were obtained by approximating the long-time density transient with a single exponential function

$$\delta\rho(z,t) = \delta\rho(z,\infty) + A(z)\exp(-t/\tau) \tag{15}$$

and the values were found to be quite reproducible. This reversibility of the entire profile appears to exclude convec-

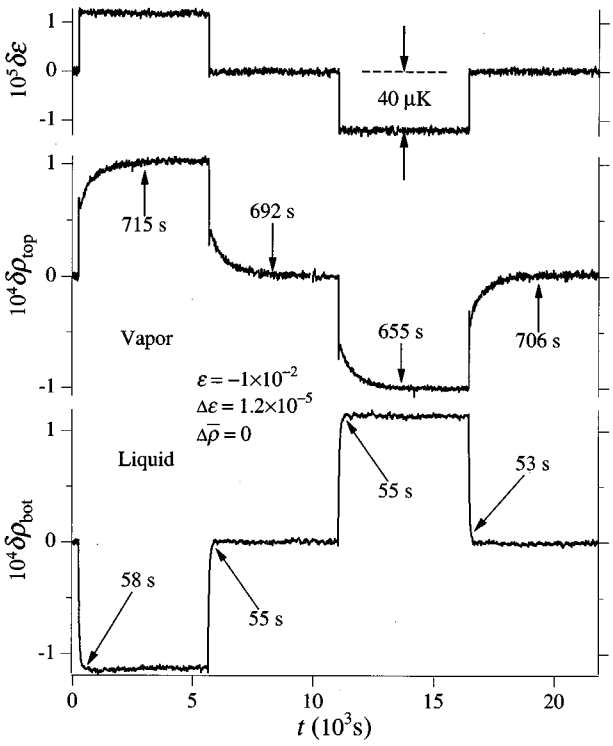

FIG. 5. Experimental observations of the temperature step sequence and the density temporal profiles in the liquid and vapor phases of ^{3}He for $\epsilon = -1\times10^{-2}$, $\Delta\epsilon = \pm1.2\times10^{-5}$, and $\Delta\overline{\rho} = 0$. The numbers tagged on the curves represent τ_{eff}.

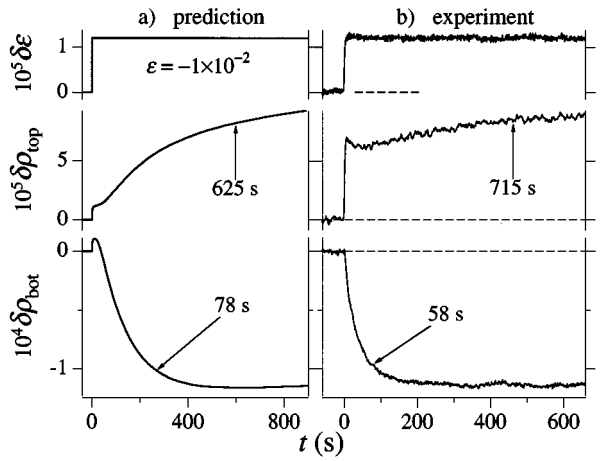

FIG. 6. Density temporal profiles from the same temperature step sequence as in Fig. 5, but expanded in time, and compared with corresponding computer simulations. The numbers tagged on the curves represent $\tau_{\rm eff}$.

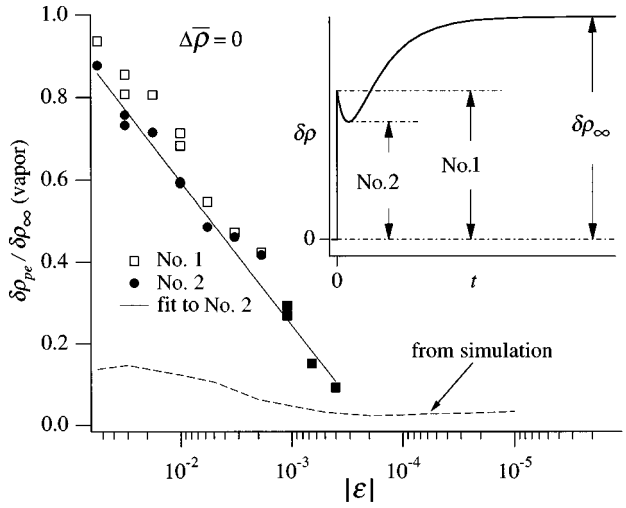

FIG. 7. Ratio $\delta\rho_{pe}/\delta\rho(\infty)$ in the vapor phase from experiments as a function of reduced temperature and for $\Delta\overline{\rho}=0$. The inserted schematic temporal profile defines the amplitudes of $\delta\rho_{pe}$ of the first peak (No. 1 open squares) and of the minimum (No. 2 solid circles). For $|\epsilon|<2\times10^{-3}$ the difference between the two amplitudes cannot be resolved. The simulation does not show the minimum but a plateau with a small slope. The dashed line is taken at the foot of the plateau.

tion effects at these small steps of $\Delta\epsilon$. The expanded portion of the early transient for a positive temperature step in Fig. 5 is shown in Fig. 6 and is compared with the simulated transient of the same temperature step change. Several aspects should be noted.

First, there is fair qualitative agreement between simulation and experiment in that they both show the striking differences between the liquid and vapor phases. When Eq. (15) is used to analyze the simulated transients for the remaining $\sim1/3$ of the total density change and in the same way as for the experiments, the effective relaxation times are found to be $\tau_{\rm eff}({\rm liq})=78$ s and $\tau_{\rm eff}({\rm vap})=625$ s, which compares with the experimental values $\tau_{\rm eff}=55$ and 700 s. The difference between the liquid and vapor phases is understood from the simulation as the consequences of (i) the stronger piston effect in the vapor phase and (ii) the undershoot caused by the expanding boundary layer of the liquid phase. As one can see from Fig. 4, the attempt to measure the asymptotic relaxation time from the liquid density transient is limited by the experimental resolution (marked by the double-arrowed horizontal line): what the experiment can measure is effectively the portion of the transient that precedes the undershoot and leads to a much shorter time than the asymptotic relaxation time τ. On the other hand, τ can be better approximated from the measurement in the vapor phase, even though the finite instrument resolution leads to an effective relaxation time larger than the asymptotic one.

Second, there are systematic differences at short times between simulation and experiment. In the vapor phase, the experiment shows a considerably larger initial sharp rise than does the simulation. In the liquid phase, the experiment does not show the predicted initial sharp rise and maximum.

As $|\epsilon|$ is increased, the observed density profiles $\rho_{\rm vap}(t)$ show a systematic trend whereby the relative amplitude of the sharp increase $\delta\rho_{pe}$ (for ''piston effect'') immediately after the step $\Delta\epsilon$ becomes larger and eventually nearly equals the total change $\delta\rho(\infty)$. The computer simulation results for the profile $\rho_{\rm vap}(t)$ and for $\rho_{\rm liq}(t)$, by contrast, do not show a substantial temperature dependence for $|\epsilon|>1\times10^{-2}$. Figure 7 illustrates the temperature dependence of the ratio $\delta\rho_{pe}/\delta\rho(\infty)$ in the vapor phase, as obtained from experiments and simulations. The straight line in the graph is a fit of $a+b\log_{10}(|\epsilon|)$ to the data of No. 2 defined in the graph with $b=0.35$, a value that happens to be close to the effective critical exponent β. We note that $\delta\rho_{pe}/\delta\rho(\infty)\simeq0$ for $|\epsilon|<2\times10^{-4}$. The ratio from the simulation is much smaller than in the experiments for $|\epsilon|>5\times10^{-4}$. Here the change $\delta\rho_{pe}$ is that of the plateau after the sharp initial rise shown in Fig. 6.

2. Stratified coexisting phases

In Fig. 8 the experimental observations after two consecutive $\Delta\epsilon$ steps at $\epsilon=-1\times10^{-3}$ are shown and the profiles are again found to be quite reversible upon a sign change of $\Delta\epsilon$. The shapes in the late equilibration stage of the observed density transients in both the liquid and vapor phases, of opposite sign, have become more similar, resulting in more comparable effective relaxation times. The experimental observations are compared with the simulation results for $\Delta\epsilon>0$. As can be seen from Fig. 8, the simulation takes a much longer time to approach equilibrium than the experiment does. In the simulation, the amplitude ratio of the sharp initial rise $\delta\rho_{pe}$ to the total density change $\delta\rho_{\rm vap}(\infty)$ in the vapor has half the size of that for $\epsilon=-1\times10^{-2}$. By contrast, this amplitude ratio for the experimental $\delta\rho_{\rm vap}(t)$ is considerably smaller than at larger $|\epsilon|$, as shown in Fig. 7.

As $|\epsilon|$ becomes smaller than 1×10^{-3}, the simulation shows quite different spatial profiles from those at $\epsilon=-1\times10^{-2}$ at various times: the amplitude ratio of the temperature overshoot in the vapor phase over the temperature inhomogeneity in the liquid phase is much larger; smaller diffusivity reduces the role that the expanding boundary layers play, thus there is no visible undershoot in the temporal evolution of the density in the liquid phase; the

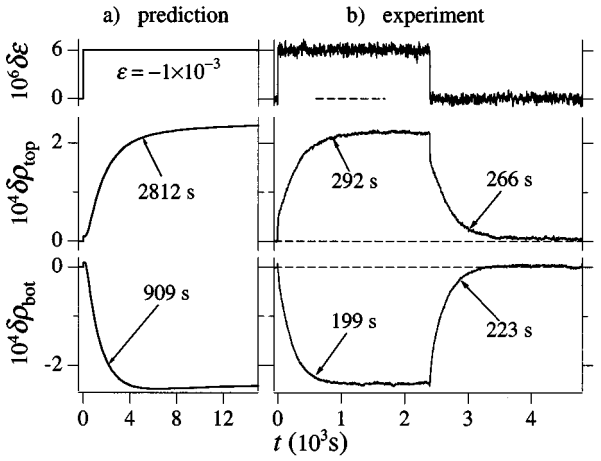

FIG. 8. Density temporal profiles in the liquid and the vapor phases after temperature steps $|\Delta\epsilon| = 6\times10^{-6}$ at $\epsilon = -1\times10^{-3}$ and for $\Delta\overline{\rho} = 0$. The computer simulation for $\Delta\epsilon > 0$ is shown on the left-hand side. The observed data after two consecutive temperature steps in opposite directions are on the right-hand side.

density change at equilibrium shows the effect of large stratification change. The experimental observations of the density transients after two consecutive $\pm\Delta T$ steps show the profiles to be quite reversible, which seems to exclude any obvious convection effects. Here the contribution from the sharp initial response to the total density change is no longer observed in the vapor phase and the density temporal profiles for the sensors at the location of the liquid and vapor phases are closely the same.

3. Time constants and data discussion

In Fig. 9 we present the predicted relaxation times. Because it is interesting to compare the results for the regimes of single phase and coexisting phases, we have also presented in the same figure the results obtained previously for $\epsilon > 0$ [6]. Here we discuss three types of relaxation times.

(a) The asymptotic time τ. This time is obtained by fitting the simulated $|\rho - \rho_\infty|$ over the available straight portion as shown in the semilogarithmic plot of Fig. 4. For equilibration under normal gravity, both curves coming from opposite directions ($\epsilon < 0$ and $\epsilon > 0$) join smoothly at T_c. Under microgravity conditions, both curves diverge at T_c (dot-dashed lines).

(b) The estimated asymptotic time $\tau_{\rm est}$. The purpose of introducing this time is to obtain a physical interpretation for and a check on the τ from the simulations. In a single-phase fluid under conditions of constant $\overline{\rho}$ and for times $t > \gamma^2 t_1$, Onuki and Ferrell [11] predict an exponential decay of the temperature transient with a relaxation time given by

$$\tau = \frac{h^2}{A\pi^2 D_T}, \tag{16}$$

where A is a function of γ varying from $A=4$ for $\gamma \gg 1$ to $A=1$ for $\gamma = 1$ [19]. If the equilibrium is approached under the condition of constant pressure instead of constant average density, the coefficient would be $A=1$ independent of the value of γ. We have obtained for $T > T_c$ a good estimate of the relaxation time we define as $\tau_{\rm est}$ by using Eq. (16) with the D_T replaced with its spatial average when a strong density stratification is present and the result is shown in Fig. 9. We note that this estimate is in good agreement with the τ from simulations when the stratification is small and both exhibit the leveling off of the asymptotic relaxation as T approaches T_c in presence of the Earth's gravity.

For the two-phase system, we use again a spatial average of D_T in Eq. (16) with $A=4$ (implying $\gamma \gg 1$) as an estimate for τ of the overall equilibration. The result is also shown as $\tau_{\rm est}$ in Fig. 9. In contrast to the result of the single phase, the estimation based on Eq. (16) is significantly lower than the τ obtained from the simulation, by a factor varying from 1.7 at $|\epsilon| = 1\times10^{-5}$ to 5.0 at $|\epsilon| = 8\times10^{-2}$ for $g = g_0$, as shown by the solid line in Fig. 10. One possible explanation for this discrepancy might be that in the two-phase system, the volume of each phase can change at the expense of the other while their total volume remains constant. This is visualized in Fig. 18 of Appendix C, which shows the meniscus motion after the temperature step change. Since equilibration does not proceed under conditions of strictly constant volume for each phase, we anticipate a change of the factor A in Eq. (16) from its value of 4.

The main reason for the variation of $\tau/\tau_{\rm est}$ with $|\epsilon|$ is the oversimplification of using the average of the local D_T in the calculation of $\tau_{\rm est}$. For $|\epsilon| > 1\times10^{-3}$, $\tau/\tau_{\rm est}$ is larger than 4 because of the approximation of $\gamma \gg 1$. A proper accounting of γ will raise $\tau_{\rm est}$, hence lower $\tau/\tau_{\rm est}$. This effect was not included in our calculation of $\tau_{\rm est}$. For $|\epsilon| < 1\times10^{-3}$, where one can use $\gamma \gg 1$ to a very good approximation, $\tau/\tau_{\rm est}$ becomes smaller than 4 because of the spatial average of D_T fails to describe qualitatively the effect of stratification on the equilibration. When a simulation under microgravity

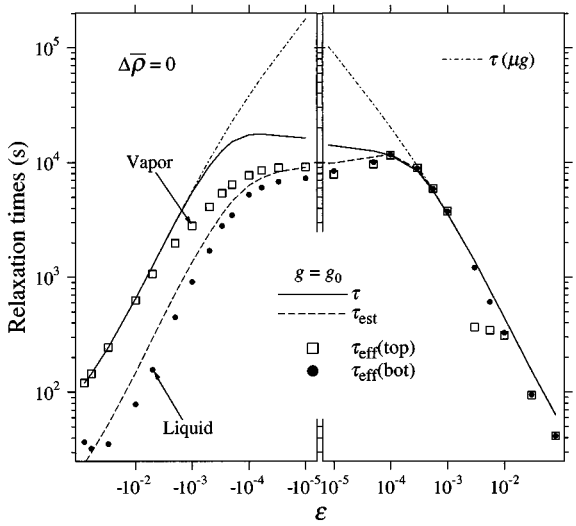

FIG. 9. Computed relaxation times versus the reduced temperature, both below and above T_c. The symbols are $\tau_{\rm eff}$ obtained from the density transients at the top and bottom sensors as explained in the text. The solid lines are the asymptotic times τ obtained from the simulations. The dashed lines are the relaxation times $\tau_{\rm est}$ from Eq. (16). The above are under normal gravity. The dot-dashed lines are τ under a reduced gravity of $g = g_0\times10^{-6}$.

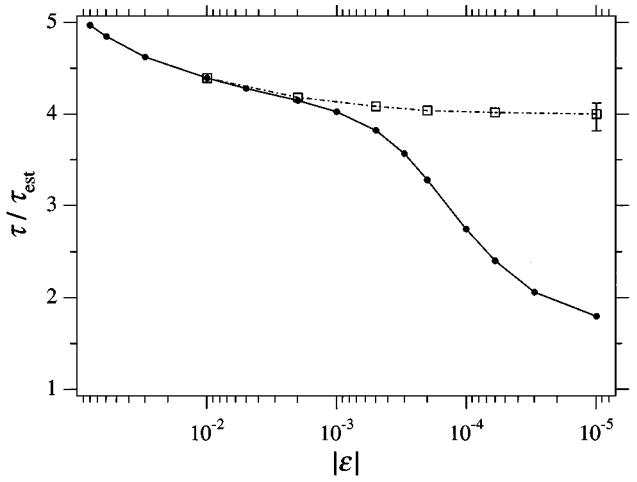

FIG. 10. Ratio of the relaxation times τ/τ_{est} along the critical isochore, where τ is from simulations and τ_{est} is calculated as described in the text. Solid circles, under normal gravity $g=g_0$; open squares, under microgravity conditions with $g=g_0\times10^{-6}$.

conditions is performed and both τ and τ_{est} diverge, the ratio τ/τ_{est} tends to 4.0 as $|\epsilon|\to0$ (dot-dashed line with open squares in Fig. 10).

(c) The effective relaxation time τ_{eff} at the location of the top (vapor) and bottom (liquid) sensors. Shown also in Fig. 9 are the values of τ_{eff} at the sensor locations, obtained by fitting Eq. (15) to the simulated density transients over the last 1/3 of the total density change. As we have seen from Figs. 2 and 4, the τ_{eff} from the liquid phase is affected by the density undershoot that is caused by the diffusion of the boundary layer. Therefore it is purely accidental that τ_{eff}(liquid) coincides with τ_{est} over a wide temperature range. We note that the τ_{eff}(vapor) follows the asymptotic relaxation time τ closely for $|\epsilon|>5\times10^{-3}$.

In Fig. 11 the effective relaxation times obtained from the experiment are presented both below and above T_c for comparison, together with the simulated data. In contrast to the single-phase regime above T_c, the experiments indicate two time scales, for the liquid and the vapor, respectively, which join near $\epsilon=-1\times10^{-3}$ as T_c is approached. One of the time scales diverges with decreasing $|\epsilon|$, with a similar power exponent as in the single phase, while the other decreases. Both times then increase and level off as $|\epsilon|$ tends to zero and join those from the single phase at T_c.

Both the τ_{eff}(vapor) and τ_{eff}(liquid) obtained from the simulations increase as T_c is approached. Therefore a significant discrepancy exists between experiments and simulations below T_c, particularly in the regime $|\epsilon|>1\times10^{-3}$, where stratification is small. We note that it is in this regime that τ_{eff} and the ratio $\delta\rho_{pe}/\delta\rho_\infty$ in the vapor phase show strong differences from simulations and we suspect that their behavior must be correlated. Both these quantities show a marked decrease with decreasing $|\epsilon|$. Hence the situation below T_c differs appreciably from that above T_c, where the computed and observed density profiles were in good agreement, except for the time scales, and there was qualitative agreement in the trend of τ_{eff} with ϵ.

There is another discrepancy between the simulation and measurement on τ_{eff} in the region of small $|\epsilon|$ with large

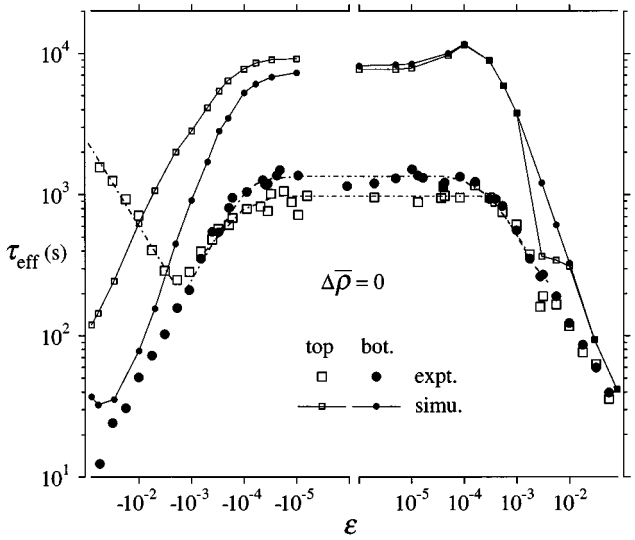

FIG. 11. Relaxation times τ_{eff} determined from the top and bottom sensors versus the reduced temperature, both below and above T_c. Below T_c the symbols represent the relaxation times in the vapor (squares) and liquid (solid circles): Larger symbols, experiments; smaller symbols, simulations. The various lines (solid and dot-dashed) are guides to the eye.

stratification. In the simulation, τ_{eff}(top) is shorter than τ_{eff}(bottom) for $T>T_c$. This is explained as the influence of the temperature overshoot on the density transient near the cell top [6]. On the other hand, for $T<T_c$, the influence in the liquid phase of the diffusing boundary layer on the density transient is stronger than the influence of the temperature overshoot in the vapor phase. Therefore τ_{eff}(bottom) for the liquid is shorter than τ_{eff}(top) for the vapor. However, by contrast, the measurements show that τ_{eff}(top) is shorter than τ_{eff}(bottom) for both $T>T_c$ and $T<T_c$.

B. Isotherms

We have discussed the possible reasons for the qualitative disagreement in relaxation times between the simulation and experimental observation along the critical isochore. The spatial profiles of $\rho(z,t)$ and $\epsilon(z,t)$ when equilibrium is approached and the heat generation (or absorption) at the meniscus are two key factors. The simulation along isotherm reveals more about these two factors since the meniscus location and the heat generated or absorbed at the meniscus are functions of the fluid average density.

Here we present two extreme situations. In the first one at $\epsilon=-1\times10^{-2}$, there is no stratification within each phase, although there is a phase separation under the Earth's gravity. The two phases coexist in the cell throughout the investigated region $-0.17<\Delta\overline{\rho}<0.09$. In the second, at $\epsilon=-3\times10^{-4}$, stratification is important within both phases and also the coexistence regime exists only for $|\Delta\overline{\rho}|<0.08$. Here we will see dramatic changes occurring in both the spatial and temporal density profiles—and therefore in the relaxation times—when meniscus and latent heat are removed. Along both isotherms, discontinuities or sharp extrema in τ_{eff} are predicted and observed at a sensor when the meniscus approaches and leaves the location of this sensor as $\Delta\overline{\rho}$ varies.

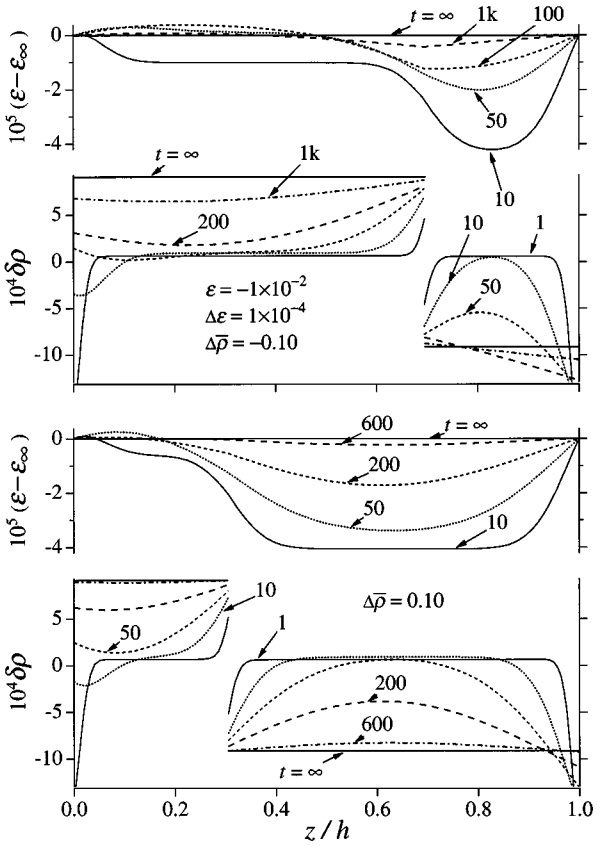

FIG. 12. Simulated spatial profiles of $\epsilon-\epsilon_\infty$ and $\delta\rho$ at various times (in s). The simulations are made along an isotherm of $\epsilon=-1\times10^{-2}$ with a temperature step $\Delta\epsilon=1\times10^{-4}$ for two average densities $\Delta\overline{\rho}=-0.10$ and $\Delta\overline{\rho}=0.10$.

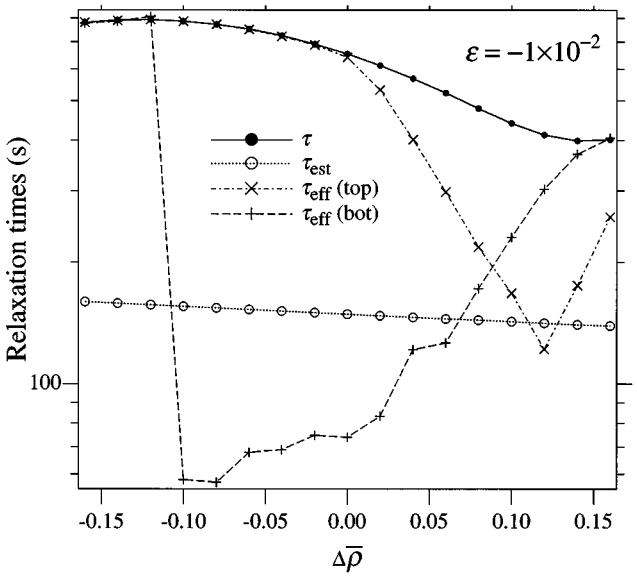

FIG. 13. Computed relaxation times from the simulations along the isotherm of $\epsilon=-1\times10^{-2}$. The symbols + and × represent τ_{eff} obtained from the simulated density transients at the top and bottom sensors as explained in the text. The solid circles represent the asymptotic time τ obtained from the simulations. Open circles represent the relaxation times τ_{est} from Eq. (16) under normal gravity. Along this isotherm over the range $|\Delta\rho|<0.16$, the fluid has always two coexisting phases.

1. The isotherm of $\epsilon=-1\times10^{-2}$

In Fig. 12 we present the simulated spatial profiles of $\epsilon-\epsilon_\infty$ and $\delta\rho$ at various time instants for two average reduced densities $\Delta\overline{\rho}=-0.10$ and 0.10. The computations are made at $\epsilon=-1\times10^{-2}$ with a step $\Delta\epsilon=1\times10^{-4}$. Both the temperature and density spatial profiles are strongly affected by the meniscus location. For $\Delta\overline{\rho}=-0.10$, where the volume ratio of the vapor phase to that of the liquid phase is larger than for $\Delta\overline{\rho}=+0.10$, the piston effect is stronger. This results in a faster change of the average temperature for $\Delta\overline{\rho}=-0.10$ (clearly seen at $t=50$ s) and a stronger temperature overshoot in the vapor phase, as compared to the results for $\Delta\overline{\rho}=+0.10$.

The shapes of the density transients (not shown) for the two average densities are also strongly affected by the meniscus location and the difference in the magnitudes of the piston effect. A strong density undershoot appears in the liquid phase for $\Delta\overline{\rho}=-0.10$ but not for $\Delta\overline{\rho}=0.10$. Further analysis of the density transients, made in the same way as in Fig. 4, shows that an asymptotic relaxation time τ exists for the entire fluid with $\Delta\overline{\rho}\neq0$.

The computed relaxation times from the simulations along the isotherm of $\epsilon=-1\times10^{-2}$ are shown in Fig. 13. The variation of the asymptotic relaxation times τ obtained from the simulations versus $\Delta\overline{\rho}$ is larger than that of τ_{est}. The ratio τ/τ_{est} varies from 5 at $\Delta\overline{\rho}=-0.12$ to 2.8 at $\Delta\overline{\rho}=0.14$. We believe this variation to result from the oversimplified estimation of τ_{est} using spatial average of D_T, just as it was the case for the calculation of the ratio along the critical isochore.

The computed effective relaxation times obtained from the density transients at the two sensor locations are also shown in Fig. 13. For $\Delta\overline{\rho}>-0.12$ the bottom sensor measures the density of the liquid phase and for $\Delta\overline{\rho}<0.12$ the top one measures the density of the vapor phase. However, the dependence of the τ_{eff} on the $\Delta\overline{\rho}$ for both the liquid and vapor phases deviates dramatically from that of τ. We explain the behavior of τ_{eff}(liquid) as follows. As the $\Delta\overline{\rho}$ increases, the magnitude of density undershoot at $z/h=0.733$ decreases (this is related to the weaker overall piston effect), and the density transient at this location follows better the temperature transient, resulting in the increased τ_{eff}(bottom).

The temporal density profiles obtained experimentally and from the computer simulation along the isotherm $\epsilon=-1\times10^{-2}$ resemble those presented in Fig. 6. Again the observed amplitude ratio $\delta\rho_{pe}/\delta\rho_\infty$ in the vapor phase is considerably larger than in the simulations, which is of the order of 0.1. This experimental ratio is found to vary with $\Delta\overline{\rho}$ as shown in Fig. 14.

In Fig. 15 we show (a) the meniscus location calculated from Eq. (14), based on the assumed symmetric location of the sensors in the cell, (b) the densities measured by the two capacitive sensors, and (c) the effective relaxation times measured from the experimental density transients vs the $\Delta\overline{\rho}$ at $\epsilon=-1\times10^{-2}$. The bottom sensor measures the liquid density for $\Delta\overline{\rho}>-0.072$ and the vapor density for $\Delta\overline{\rho}<-0.112$. The width of the transition from the liquid to the vapor is caused by the finite sampling width (0.38 mm)

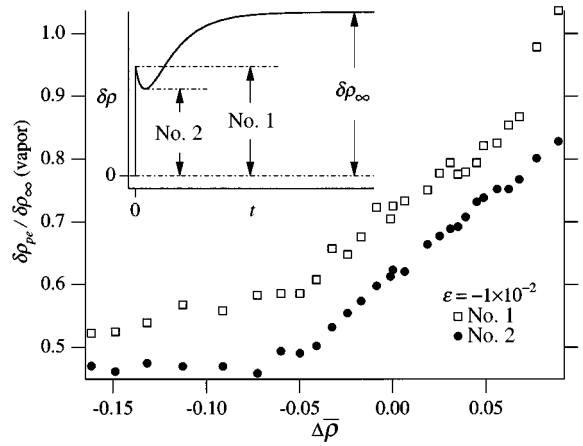

FIG. 14. Amplitude ratio $\delta\rho_{pe}/\delta\rho_\infty$ in the vapor phase from experiments as a function of average density $\Delta\overline{\rho}$ along the isotherm $\epsilon=-1\times10^{-2}$. Inset: schematic temporal profile with the amplitudes of $\delta\rho_{pe}$ defines the symbols for the first peak (No. 1, open squares) and the minimum (No. 2, solid circles).

of the capacitive sensor when the meniscus moves across it, which is indicated by the two dashed lines in graph (a). The discrepancy between the predicted and measured density transitions versus $\Delta\overline{\rho}$ is explained if the location of the pair of the sensors is not exactly symmetric in the cell, but moved upward by 0.2 mm. It is interesting that the transition width of the measured effective relaxation time is larger than that from the equilibrium density measurement. We interpret this observation with the help from Fig. 12. Besides the cell

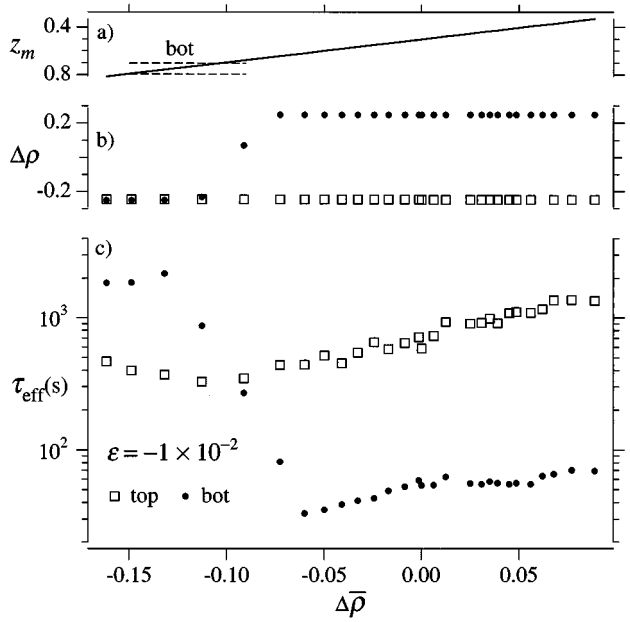

FIG. 15. (a) Meniscus location, calculated from Eq. (14), versus $\Delta\overline{\rho}$. The dashed lines indicate the physical location of the bottom sensor with the distance between the dashed lines representing the finite sampling width of the sensor. (b) Reduced density measured by the two sensors vs $\Delta\overline{\rho}$. (c) The effective relaxation times $\tau_{\rm eff}$ along the isotherm of $\epsilon=-1\times10^{-2}$, determined from the top and bottom sensors versus $\Delta\overline{\rho}$. Solid circles, bottom sensor; open squares, top sensor.

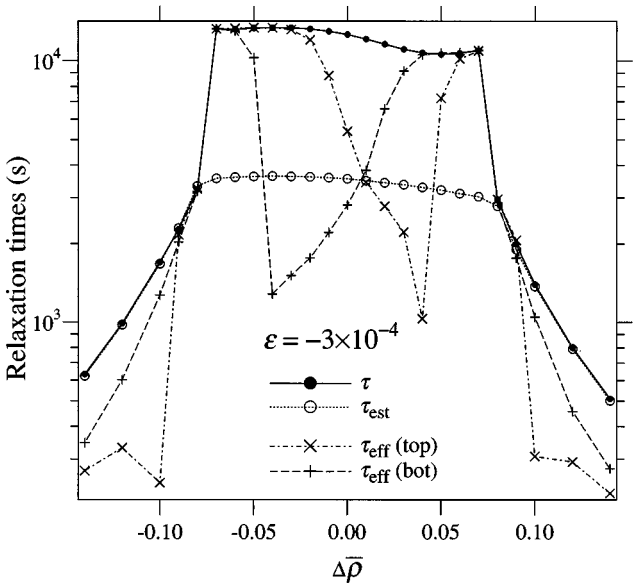

FIG. 16. Computed relaxation times from the simulations along the isotherm of $\epsilon=-3\times10^{-4}$. The two phases coexist in the cell over $|\Delta\overline{\rho}|<0.078$. For $\Delta\overline{\rho}>-0.04$ the bottom sensor samples the liquid phase. The same holds for the top sensor at $\Delta\overline{\rho}>0.04$. The symbols + and × are $\tau_{\rm eff}$ obtained from the simulated density transients at the top and bottom sensors as explained in the text. Solid circles, asymptotic time τ obtained from the simulations, open circles, relaxation time $\tau_{\rm est}$ from Eq. (16) under normal gravity.

boundary layers, there are also the interface layers within which the density changes in the opposite directions in the liquid and vapor phases. Even though the physical location of the meniscus is outside the sensor, the effect of the interface boundary can still be felt by the sensor via the interface layers. Therefore the ''dynamic response width'' is larger than the ''static transition width.'' For $\Delta\rho>-0.06$, the $\tau_{\rm eff}$ in both phases increases with increasing $\Delta\overline{\rho}$ and their ratio remains nearly constant. The behavior of the $\tau_{\rm eff}$(liquid) from the experiment agrees with that from the simulation (see Fig. 13). However, the experimental $\tau_{\rm eff}$(vapor) increases with the increasing $\Delta\overline{\rho}$ for $-0.12<\Delta\overline{\rho}<0.08$, while the simulated $\tau_{\rm eff}$(vapor) varies in the opposite direction in the same range. Here again, experiment and prediction do not agree, as was found along the critical isochore for $|\epsilon|>10^{-3}$. We note again that both the experimental $\tau_{\rm eff}$ and the ratio $\delta\rho_{pe}/\delta\rho_\infty$ in the vapor phase decrease as $\Delta\overline{\rho}$ decreases. Hence there must be a correlation between the large ratio $\delta\rho_{pe}/\delta\rho_\infty$ and the long $\tau_{\rm eff}$ from experiments, both quite different from the predictions, for the isotherm of $\epsilon=-1\times10^{-2}$ as well as for the critical isochore as was described before.

2. The isotherm of $\epsilon=-3\times10^{-4}$

In Fig. 16 we show the computed relaxation times from simulations for $\epsilon=-3\times10^{-4}$. Here the meniscus disappears at the top and bottom boundaries at about $|\Delta\overline{\rho}|=0.078$. The discontinuity both in the $\tau_{\rm eff}$ and the τ at this value of $\Delta\overline{\rho}$ is an important indication that the existence of the meniscus is the bottleneck of the equilibration. In the absence of a meniscus in the cell, the equilibration proceeds much faster than in its presence and the asymptotic τ agrees well with $\tau_{\rm est}$

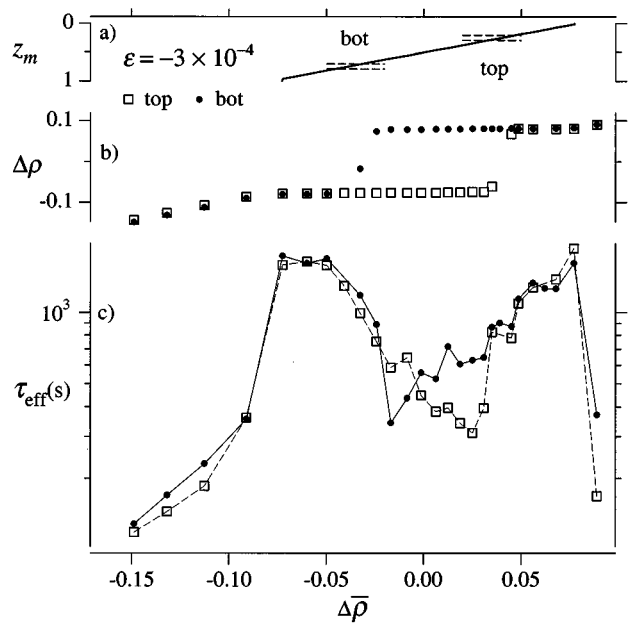

FIG. 17. (a) Meniscus location, calculated from Eq. (14), versus $\Delta\overline{\rho}$ along the isotherm $\epsilon = -3\times10^{-4}$. The dashed lines indicate the physical locations of the sensors with the distance between the dashed lines representing the finite sampling width of the sensors. The region of $0<z_m<1$ identifies the regime of coexisting phases. (b) Experimental reduced density measured by the two sensors vs $\Delta\overline{\rho}$. (c) Observed effective relaxation times $\tau_{\rm eff}$ determined from the top and bottom sensors versus $\Delta\overline{\rho}$. Solid circles, bottom sensor; open squares, top sensor. The solid and dashed lines are guides to the eyes.

from Eq. (16) with $A=4$, which is for equilibration at constant total volume. In the presence of the meniscus, τ is larger than $\tau_{\rm est}$ by a factor of about 4, as if equilibration proceeded at constant pressure, namely, with $A=1$ in Eq. (16), though the total volume remains constant, as we already discussed in Sec. V A 3.

As the average fluid density $\Delta\overline{\rho}$ is changed and the equilibration location of the meniscus is moved vertically across the cell, the effective relaxation times $\tau_{\rm eff}$ at the two sensor locations are strongly affected by the proximity of the meniscus. This is the result of the interplay of the thermal diffusion in the bulk fluid and the diffusing boundary layer at the meniscus, which operates very much in the same manner as near the boundary of the cell. Thus the density transient appears accelerated, generating a smaller $\tau_{\rm eff}$, as evidenced by sharp minima in $\tau_{\rm eff}$ vs $\Delta\overline{\rho}$.

Figure 17 shows the experimental $\tau_{\rm eff}$ versus $\Delta\overline{\rho}$ for the isotherm of $\epsilon=-3\times10^{-4}$. Here the meniscus position is more sensitive to changes of $\Delta\overline{\rho}$ than at $\epsilon=-1\times10^{-2}$: over the density range covered in our series of experiments, upon decreasing $\Delta\overline{\rho}$ the meniscus enters the cell at the top, passes the location of both the top and the bottom sensor, and leaves the cell at the lower cell boundary. Therefore simulations predict dramatic changes of the relaxation times. The measured temporal density profiles at both sensors indicate discontinuities in $\tau_{\rm eff}$ at the appearance of the meniscus in the cell and its disappearance and a sharp anomaly as the meniscus approaches and then passes each respective sensor location. The agreement in the overall behavior of $\tau_{\rm eff}$ vs $\Delta\rho$ between the experimental and the simulated results along this isotherm is encouraging.

Finally, we note the good agreement between the predicted and observed meniscus positions in Figs. 17(a) and 17(b). The disappearance of the meniscus for $|\Delta\overline{\rho}|>0.078$ is marked by a departure of $\Delta\rho$ from a near constant value, as expected.

VI. SUMMARY

In this paper we have presented a theoretical and an experimental study of the local density change $\delta\rho(z,t)$ inside a two-phase pure fluid at constant volume in the region below the liquid-vapor critical point. This study was carried out with ^{3}He and the experiment was performed in a flat cylindrical cell with two superposed density sensors. In most cases, the top and the bottom sensors measure, respectively, the vapor and liquid density. The experiments produce an effective relaxation time $\tau_{\rm eff}$ by approximating the tails of the density transients by a simple exponential decay. Computer simulations predict the spatial and temporal profiles of $\delta\rho(z,t)$, which lead to the prediction of $\tau_{\rm eff}$ and also of the asymptotic relaxation time τ that is not often observable because of the finite signal-to-noise ratio of the apparatus. Studies were performed along the critical isochore and two isotherms. The principal results are as follows.

(i) The simulations show that there exists an asymptotic relaxation time τ for the entire two-phase coexisting system even though the thermodynamic properties of each phase are quite different. This τ is larger by a factor of the order of 4 than the estimated time $\tau_{\rm est}$ based on the average thermal diffusivity taken over the entire fluid sample and derived under the assumption of constant volume. Our study of the ratio $\tau/\tau_{\rm est}$ along the critical isochore and along isotherms, both with and without stratification from gravity, indicates that the fluid behaves as if each phase relaxes at constant pressure, even though the total system relaxes at constant volume.

(ii) The simulations predict a rapid density change $\delta\rho_{pe}(t)$ from the piston effect within each phase in the same direction, immediately following a temperature step change $\Delta\epsilon$. The magnitude of $\delta\rho_{pe}(t)/\Delta\epsilon$ varies slightly with the reduced temperature along the critical isochore. This rapid density change is observed experimentally in the vapor phase but with a much larger amplitude than predicted. By contrast, it is hardly observable in the liquid phase. We tentatively attribute the disagreement between experiment and prediction to two assumptions made in the simulation: (a) There is no meniscus motion in the acoustic time regime and (b) the meniscus temperature is solely determined by the saturation vapor pressure at any time.

(iii) For $|\epsilon|>1\times10^{-3}$, the vapor appears to equilibrate more slowly than the liquid. This leads to the $\tau_{\rm eff}$(liquid) to be shorter than $\tau_{\rm eff}$(vapor). The simulated spatial and temporal profiles reveal the causes of the puzzle and show that the diffusing boundary layers have a stronger impact on the density equilibration in the interior of the liquid phase than in the vapor. The observed $\tau_{\rm eff}$ reflects these dynamics. Because the density detector has a finite resolution, it cannot

resolve the very small density variation in the asymptotic regime.

(iv) The simulation shows that along the critical isochore both the $\tau_{\rm eff}$ and τ first diverge as T_c is approached and then roll over to a constant value because of fluid stratification in the cell. The behavior of the experimental $\tau_{\rm eff}$(liquid) agrees qualitatively with the isochore simulation. By contrast, when T_c is approached from $|\epsilon|=0.1$, $\tau_{\rm eff}$(vapor) first decreases and then increases until it levels off.

(v) The simulations and experiments along two isotherms give insight into the equilibration processes as a function of average density over the range of $-0.15<\Delta\overline{\rho}<0.15$. By changing the $\Delta\overline{\rho}$, the meniscus position z_m is made to vary through the cell, passing one or both sensors and finally reaching the cell boundary. This leads to striking changes in the experimental and simulated relaxation times. Especially when the meniscus moves out of the cell boundary, the system equilibrates much faster, indicating that at times of the order of τ the thermal equilibration changes from a ''constant pressure'' to a ''constant volume'' condition.

(vi) Simulations of the density changes under microgravity conditions show that $\tau_{\rm eff}$ and τ continue to diverge instead of leveling off as T_c is approached.

The disagreements for the vapor phase, both in the temporal profile and in $\delta\rho$(vapor,t) and in $\tau_{\rm eff}$(vapor) between the experiment and prediction in particular for $|\epsilon|>1\times10^{-3}$ are not understood. Some plausible suggestions have been advanced and possible shortcomings in theory were pointed out. New experimental data that we expect to take with a cell of simpler, more ideal geometry and insulated side walls might give a more favorable comparison with the 1D simulations.

ACKNOWLEDGMENTS

This research has been supported by NASA Grants Nos. NAGW-3328 and NAG5-379. The authors are very indebted to L. Eicher for discussions, for helpful advice on a computer problem occurring during the simulation, and also for a copy of his own simulation paper on CO_2 prior to publication. The authors are also indebted to B. Zappoli for a copy of his work prior to publication and helpful correspondence. Numerous discussions with D. Murphy are also acknowledged.

APPENDIX A: FLOW VELOCITY AND CONVECTION

In presence of gravity, the possible onset of convection needs to be considered. As shown in Fig. 3 of [6] for $\Delta T>0$ in the intermediate regime for times $t>t_1$, the bottom half of the cell has a negative spatial density gradient, which renders this portion of the fluid mechanically unstable, and should start convection, while the top half of the fluid is stable. Conversely, for an inverted step $-\Delta T$, it is the top portion of the cell that becomes mechanically unstable.

A calculation of the convective motion is not possible in the simulation of both the present paper and a previous one [6] because the numerical solution is sought only in one dimension. It is argued that convection effects must be small on the basis of experimental data: When the temperature step ΔT was inverted, nearly the same temporal profile $\rho(t)$ was observed at two superposed locations where the density was sampled. Also it is argued that for $t>t_1$ the remaining temperature gradients in the fluid under the experimental conditions were well below that for convection onset.

Zappoli and co-workers [16] have carried out a detailed numerical calculation of mass transport in a square cavity filled with fluid CO_2 at $\epsilon=3\times10^{-3}$. In their 2D geometry, the temperature of one vertical boundary is changed by ΔT while the three other sides are thermally insulated. The computations showed the signature of the piston effect over a time of the order of t_1 during which large density gradients and a vertical buoyant velocity component develop at the boundary. This vertical buoyant velocity drives the bulk motion by viscous coupling and does not change significantly the thermal structure of the boundary layer, thus the piston effect is almost convection independent. In the following slow equilibration phase, which in the absence of convection should have a relaxation time of order of τ, a convective motion develops under gravity out of the large density gradients left by the piston effect and relaxed slowly with diffusion in the quasi isothermal portion of the fluid. This convective motion shortens the effective relaxation time and its intensity decreases slowly in a time of the order of τ. Therefore Zappoli *et al.* conclude that in a fluid near the critical point, thermal and mass equilibration processes are nearly uncoupled and the piston effect is responsible for 85% of the temperature equilibration in a short time scale, while convection and diffusion homogenize the density on a much longer time scale. The detailed calculations on how much the density equilibration is shortened by the quasi steady isothermal critical convection have not yet been performed [20].

Even though the geometry used in the calculation of [16] is different from that used in [6], where the heating of the flat cell was from all the directions, their general conclusions should still apply to our experiments on ^{3}He. It is therefore of great interest to find out whether the discrepancy between the predicted and observed time constants in the ^{3}He experiments is the result of convection, in spite of the argument made on the reversible temporal density profiles for temperature steps in opposite directions.

APPENDIX B: NUMERICAL PROCEDURES

The coupled equations for temperature, pressure, and density are solved through iteration. The detailed iteration procedure to update the solution from nth time to $(n+1)$th time is as follows.

(i) Estimate $\partial P/\partial t$ and $\partial z_m'/\partial t$ from their respective temporal histories, where the subscript m is for ''meniscus.''

(ii) Calculate

$$P_0^{(n+1)}=P_0^{(n)}+(\partial P/\partial t)dt, \tag{B1a}$$

$$z_m'^{(n+1)}=z_m'^{(n)}+(\partial z_m'/\partial t)dt, \tag{B1b}$$

$$P_m^{(n+1)}=P_0^{(n+1)}+gz_m'^{(n+1)}. \tag{B1c}$$

(iii) Calculate $T_m^{(n+1)}$ from $P_m^{(n+1)}$, assuming that the temperature at the meniscus is solely determined by the saturation vapor pressure line $P_{\rm sat}=f(T)$.

(iv) Solve Eq. (5) for the temperature distribution at the $(n+1)$th time in each phase separately, using the implicit scheme, the known boundary temperatures, and the latest available $\partial P/\partial t$.

(v) Calculate $\partial z'_m/\partial t$ from Eq. (12) using the temperature distribution, latent heat, density, and conductivity at the $(n+1)$th time. Update $z'^{(n+1)}_m$ and $P^{(n+1)}_m$ using Eq. (B1).

(vi) Calculate the density distribution $\rho(z',t)$ from the equation of state using the temperature $T(z',t)$ and pressure $P(z',t)$ distributions at the $(n+1)$th time, following which the static and dynamic coefficients are updated.

(vii) Reevaluate the distribution of the grid points in the laboratory coordinate $\{z\}$ from

$$z=\int_0^{z'}\frac{dz''}{\rho(z'',t)}, \tag{B2}$$

especially

$$h_{\rm cal}=\int_0^{z'^{(n+1)}_m}\frac{dz'}{\rho_{\rm vap}}+\int_{z'^{(n+1)}_m}^{M}\frac{dz'}{\rho_{\rm liq}}. \tag{B3}$$

(viii) If the absolute value of $\Delta f\equiv(h_{\rm cal}-h)$ is smaller than a preset tolerance, the iteration is stopped. Otherwise $\partial P/\partial t$ is corrected using the Newton method with the derivative constructed of the last and current $\partial P/\partial t$ and Δf in the iteration. Then the iteration is repeated from step (ii).

The objective of the iteration is to seek a unique $\partial P/\partial t$ while the temperature and pressure distributions affected by the $\partial P/\partial t$ will generate the density distribution that maintains the total volume unchanged at the $(n+1)$th time. Usually no more than five iterations are needed for the tolerance of 1×10^{-14}. The calculated average density over the cell is within 1×10^{-12} of the known value. Then the temperature, pressure, and density at fixed spatial locations are interpolated from their respective distributions for use in computing the temporal profiles.

We estimate the initial $\partial P/\partial t$ via the heat input at two boundaries, which in turn can be approximated by the spatial derivative of the error function, the simplest solution to the 1D temperature distribution; thus

$$\left(\frac{\partial P}{\partial t}\right)_{\rm guess}\sim 2\left\langle\left(\frac{\partial P}{\partial T}\right)_\rho\right\rangle\frac{\lambda_b}{\langle\rho C_V\rangle}\frac{\Delta T}{h\sqrt{\pi(D_T)_b dt}}. \tag{B4}$$

This initial guess gives a value of $\partial P/\partial t$ that is usually within a factor of 3 from the final $\partial P/\partial t$ after iterations.

APPENDIX C: MENISCUS MOTION

We now discuss the motion of the meniscus under the conditions of $\Delta\overline{\rho}=0$, $\epsilon=-1\times10^{-2}$, and a positive temperature step $\Delta\epsilon=1\times10^{-4}$. Figure 18(a) shows the motion of the meniscus as a function of time. During the early transient when the pressure change rate is high, the vapor phase is compressed more than the liquid, therefore the vapor volume is reduced ($\delta z_m<0$). After the pressure increase fades out and the temperature change rates are comparable in each phase ($t\sim500$ s), the vapor volume starts to increase ($\partial z_m/\partial t>0$) due to the larger thermal expansion coefficient in the vapor; the meniscus moves backward to its initial location, as we have expected for $\Delta\overline{\rho}=0$.

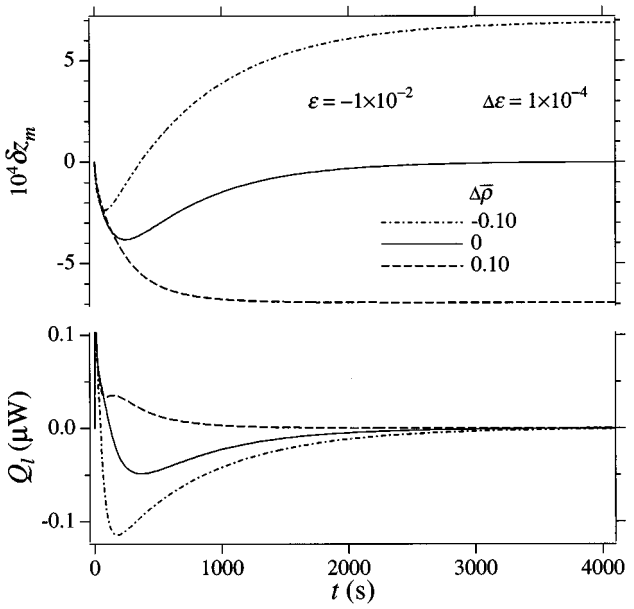

FIG. 18. Simulated temporal profiles of interface motion $\delta z_m(t)$ scaled by h (top) and the total heat $Q_l(t)$ generated at the meniscus (bottom) for three values of the average density $\Delta\overline{\rho}=-0.10$, 0, and 0.10 at $\epsilon=-1\times10^{-2}$, $\Delta\epsilon=1\times10^{-4}$, and under normal gravity.

Coupled with the meniscus motion is the mass crossing the meniscus. Because of the sharp pressure increase during the early stage, the fluid in the vapor phase near the meniscus is compressed into liquid, producing a heat source ($Q_l>0$) and accelerating the temperature increase at the meniscus. Once the thermal diffusion plays a major role in the equilibration, the mass crossing can reverse its direction towards the final equilibrium density distribution, as we have discussed in Sec. II. Then the meniscus becomes a heat sink ($Q_l<0$). In Fig. 18(b) we show the dimensionless heat produced per second $Q_l(t)$ at the interface as a function of time. As the result of the competition between the two processes, the total dynamic heat calculated from the integration of $Q_l(t)$ over t is about three times smaller than the static one calculated from the latent heat multiplied by the total mass conversion.

We have observed in the experiment a sharp and large density response following a positive $\Delta\epsilon$ step when the meniscus is inside or very close to a density sensor. As we can see from Fig. 18, when the meniscus moves rapidly towards the top boundary ($\delta z_m<0$), some vapor leaves and some liquid enters the density sensor, leading to a sharp rise of the measured density. Depending on $\Delta\overline{\rho}$, the meniscus can reverse its direction of motion, as seen from Fig. 18, with a corresponding fall of the measured density. The magnitude of the sharp density response is much larger than what could be accounted for by the piston effect on the density change in the interior fluid of each phase.

[1] H. Klein, G. Schmitz, and D. Woermann, Phys. Rev. A **43**, 4562 (1991).
[2] See, for instance, R.A. Wilkinson, R.F. Berg, M.R. Moldover, L. Eicher, J. Straub, and R.W. Gammon, in *Proceedings of the VIIIth European Symposium on Materials and Fluid Sciences in Microgravity, Brussels, 1992*, edited by B. Kaldeich (European Space Agency Publication Division, Estec, Postbus 299, 2200 AG, The Netherlands, 1992).
[3] P. Guenoun, B. Khalil, D. Beysens, Y. Garrabos, F. Kammoun, B. Le Neindre, and B. Zappoli, Phys. Rev. E **47**, 1531 (1993).
[4] J. Straub, L. Eicher, and A. Haupt, Phys. Rev. E **51**, 5556 (1995).
[5] J. Straub, A. Haupt, and L. Eicher, Int. J. Thermophys. **16**, 1033 (1995).
[6] F. Zhong and H. Meyer, Phys. Rev. E **51**, 3223 (1995).
[7] C. Pittman, T. Doiron, and H. Meyer, Phys. Rev. B **20**, 3678 (1979).
[8] C. Pittman, L. Cohen, and H. Meyer, J. Low Temp. Phys. **46**, 115 (1982).
[9] F. Zhong and H. Meyer, in *Fluid Mechanics Phenomena in Microgravity*, edited by D. Siginer, R. Thompson, and L. Trefethen (The American Society of Mechanical Engineers, New York, 1993), AMD Vol. 174, p. 139.
[10] F. Zhong and H. Meyer, in *Proceedings of the NASA/JPL 1994 Microgravity Low Temperature Physics Workshop*, edited by U. Israelson and D. Strayer (NASA/JPL, Pasadena, 1994), p. 62, experiment above and below T_c.
[11] A. Onuki and R. Ferrell, Physica A **164**, 245 (1990).
[12] P. Hohenberg and M. Barmatz, Phys. Rev. A **6**, 289 (1972).
[13] R. Courant and K. Friedrichs, *Supersonic Flow and Shock Waves* (Wiley, New York, 1948).
[14] H. Boukari, R. Pego, and R. Gammon, Phys. Rev. E **52**, 1614 (1995).
[15] J. Straub and L. Eicher, Phys. Rev. Lett. **75**, 1554 (1995).
[16] B. Zappoli, S. Amiroudine, P. Carles, and J. Ouazzani (unpublished).
[17] M. Iino, M. Suzuki, and A.J. Ikushima, J. Low Temp. Phys. **63**, 495 (1986).
[18] M. Hasan, C.S. Lin, R. Knoll, and M. Bentz (Ref. [9]), p. 125.
[19] R. Behringer, A. Onuki, and H. Meyer, J. Low Temp. Phys. **81**, 71 (1990).
[20] B. Zappoli (private communication).